

Hydrodynamics and Morphologies of Droplet Coalescence

Yongping Chen,^{*,†,‡} Chaoqun Shen,[‡] and George P. Peterson[§]

[†]School of Hydraulic, Energy and Power Engineering, Yangzhou University, Yangzhou, Jiangsu 225127, PR China

[‡]Key Laboratory of Energy Thermal Conversion and Control of Ministry of Education, School of Energy and Environment, Southeast University, Nanjing, Jiangsu 210096, PR China

[§]George W. Woodruff School of Mechanical Engineering, Georgia Institute of Technology, Atlanta, Georgia 30332, United States

Supporting Information

ABSTRACT: By the combination of high-speed imaging and numerical simulation, we explore the hydrodynamics and possible morphologies of the entire coalescence of a pendent droplet and sessile one. We identify three types of coalescence morphologies and plot a corresponding phase diagram to identify them depending on the Bond number and the size ratio between the two droplets. In addition to the well-known linear inertial growth of the liquid bridge at the initial contact of the two drops, we observe a new subsequent slower linear expansion of the liquid bridge and provide a linear scaling law with a measured prefactor to quantitatively represent it. This new growth is found to be due to the transition of the capillary force produced by a change in the azimuthal surface profile of the liquid bridge.

1. INTRODUCTION

When two separate droplets of the same fluid come into contact with each other, they typically coalesce into a single larger one to minimize the free surface energy. Significantly, the hydrodynamic behaviors during the process of this coalescence, including the rapid motion of liquid bridge formed between the two droplets, are of great scientific interest because of the richness of the underlying physics, such as free surface flow,¹ Rayleigh–Plateau instability,^{2,3} and singularity dynamics,⁴ all of which are also essential to appropriately manipulate droplet coalescence in various chemical applications.^{5–10}

Since the pioneering works of Rayleigh² and Reynolds³ on the topology changes of droplet coalescence, there have been a number of experimental and theoretical investigations undertaken to probe the dynamics of droplet coalescence. It is worth noting that the vast majority of these focused on interpreting the transient expansion of the liquid bridge during the initial stages of coalescence, and it has been demonstrated that,^{11–17} for a wide range of practical problems during coalescence within the inviscid regime, the radii of liquid bridge grows linearly with $(t^*)^{1/2}$, beginning at the moment of contact ($t^* = t/t_c$, where t is the time duration from the point at the contact of two droplets and t_c is the capillary time, defined as $t_c = (\rho R^3/\sigma)^{1/2}$, in which $R = (2R_{pi}R_{si})/(R_{pi} + R_{si})$, R_{pi} and R_{si} are the initial radii of contacting pendent and sessile droplets, respectively). In addition, by using experiments and simulations, Paulsen et al.¹⁸ reveal a new regime to describe the initial dynamics of coalescence for all drop viscosities. In this initial dynamics, all of inertial, viscous, and surface-tension forces are important. Yokota and Okumura¹⁹ observed coalescence of a viscous droplet to a bath of the same liquid confined between two plates with the distance smaller than the droplet radius in the initial stage and established a crossover dynamics which can be potentially important in various fields. Peng et al.²⁰ and Wang et al.²¹ introduced an analysis based on the energy conservation for self-propelled droplet during

coalescence on a superhydrophobic surface. A visualization experiment was conducted by Liao et al.²² for the coalescence phenomena and dynamics behavior of water droplets on an inclined surface, and it is shown that the triple-phase contact line, liquid bridge radius, and fore/back contact angle of the coalescent drop behaved as periodic damped oscillations.

However, no full information is available on the detailed morphologies and the relevant hydrodynamics during the following coalescence process, especially during the final essential pinch-off process. For this reason, by combining high speed video imaging techniques and numerical simulations, the dynamic behavior of the entire coalescence process after the contact between a pendent droplet and a sessile one is explored. Three different coalescence morphologies including two with pinch-off behavior are identified, which can be quantitatively represented by a phase diagram depending on the Bond number and the size ratio between the two droplets. Furthermore, the temporal evolution of the liquid bridge is quantitatively characterized and correlated with the corresponding governing mechanisms.

2. EXPERIMENTAL SECTION

To investigate the whole droplet coalescence process with a consideration of gravity in the air, an experiment is conducted to directly capture the rapid topological changes occurring during whole coalescence between a pendent and a sessile droplet. As illustrated in Figure 1, the stainless steel dispensing needles fixed vertically are utilized to produce a pendent droplet and a sessile one with its bulk fluid phase of water. The upper needle is fixed on a three-dimensional removable micrometer stage, an adjustment of which ensures that the

Received: April 17, 2015

Revised: August 17, 2015

Accepted: September 8, 2015

Published: September 8, 2015

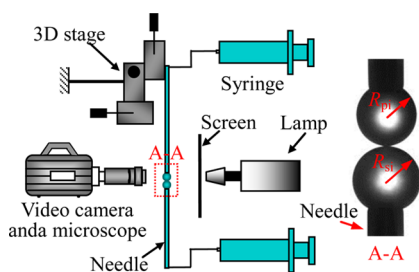


Figure 1. Schematic of experimental setup.

central coalescence between the two droplets occurs in a plumb line with negligible velocity.

In this experiment, the topography of droplet coalescence is recorded using a high-speed video camera (Photron SA4) coupled with a microscope (Zoom 160 optical system), with the recording speed of 10000 frames per second. As shown, in order to make the view field with uniform brightness, a piece of ground glass is set as a screen between the droplets and lamp. Different experimental conditions are obtained by regulating the size of the pendent and sessile droplets, which is achieved by adjusting the diameter of needles and the fluid volume supplied by the syringe. To avoid the impact of flowing air on droplet coalescence, the entire experimental apparatus is enclosed in a box with an observation window for the microscope. The room temperature is about 15 °C during the experiment.

3. NUMERICAL MODEL

3.1. Computational Domain. To gain a deep insight into the fundamental mechanism behind the different coalescence morphologies, a two-dimensional axisymmetric model is developed to provide the detailed hydrodynamic information involved in the coalescence between pendent and sessile droplets, including the velocity fields, pressure distribution, and evolution of interface. As represented in Figure 2, a rectangular

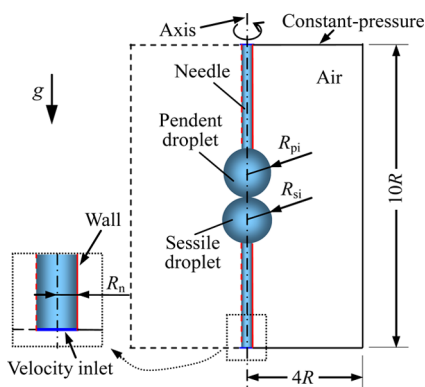


Figure 2. Schematic of computational domain.

region with the length of 10R and width of 4R is used as the computation domain. The pendent and sessile droplets are specified with the initial velocity of 0 m/s and contacted with each other at $t^* = 0$. The stationary velocity and no-slip wall condition are imposed on the inlet and needle wall, respectively. In addition, the periodical boundary conditions are set at the outer boundaries of the entire computational domain.

3.2. Mathematical Model. The volume of fluid (VOF) method is utilized to track the time-evolution of free interface.^{23,24} In each control volume, the volume fractions (α) of the two phases (liquid and air) sum to unity.

$$\alpha_l + \alpha_a = 1 \quad (1)$$

subscripts of l and a are the liquid and air, respectively. The cell with $\alpha_l = 1$ is full of the liquid phase and that with $\alpha_l = 0$ is full of the gas phase. The gas–liquid interface only exists in the cell where α_l lies between 0 and 1.

The other governing equations of the VOF formulations on gas–liquid fluid flow can be presented as follows:

Continuity equation

$$\nabla \cdot \mathbf{u} = 0 \quad (2)$$

Momentum equation

$$\rho \left(\frac{\partial \mathbf{u}}{\partial t} + \mathbf{u} \cdot \nabla \mathbf{u} \right) = -\nabla p + \nabla \cdot \mu \mathbf{S} + \rho \mathbf{g} + \mathbf{F} \quad (3)$$

where \mathbf{u} is the velocity, ρ is the density, μ is the viscosity, p is the pressure, \mathbf{S} is the strain rate tensor, and \mathbf{g} is the gravitational acceleration. The properties appearing in the equation are determined by the presence of the component phases in each control volume

$$\rho = \alpha_l \rho_l + (1 - \alpha_l) \rho_a \quad (4)$$

$$\mu = \alpha_l \mu_l + (1 - \alpha_l) \mu_a \quad (5)$$

Note that, acting as a body force (\mathbf{F}) in eq 3, the surface tension at the interface generates an additional pressure gradient, which is evaluated per unit volume using the continuum surface force method.²⁵

$$\mathbf{F} = \sigma \frac{\rho_k \nabla \alpha_a}{0.5(\rho_a + \rho_l)} \quad (6)$$

where σ is the interface surface tension coefficient and k is the free interface curvature defined as

$$k = -\nabla \cdot \left(\frac{1}{|\nabla \alpha_a|} \nabla \alpha_a \right) \quad (7)$$

The governing equations along with the boundary conditions described above are numerically solved by the control volume finite-difference technique. The pressure–velocity coupling is accomplished by the pressure-implicit with splitting of operators (PISO) coupling scheme. The pressure staggering option (PRESTO) scheme is utilized for the pressure interpolation, and the second-order up-wind differencing scheme is adopted to discretize the momentum equation. The geometric reconstruction scheme based on the piecewise linear interface calculation (PLIC) method is applied to reconstruct the vapor–liquid interface. The under-relaxation factors are used at values: 0.2 (pressure), 0.5 (density), 0.4 (body force), 0.2 (momentum) to obtain a good convergence.

On the basis of the spatial and temporal convergence tests, simulations are done under uniform grid size $\Delta x = \Delta y = 4.5 \times 10^{-3} R$ and time step, Δt , being $1.8 \times 10^{-4} t_c \sim 2.3 \times 10^{-3} t_c$ to warrant the reliable numerical results. As shown in Figure 3, the good agreement between numerically predicted results and experimental data shows the reliability of the presented model.

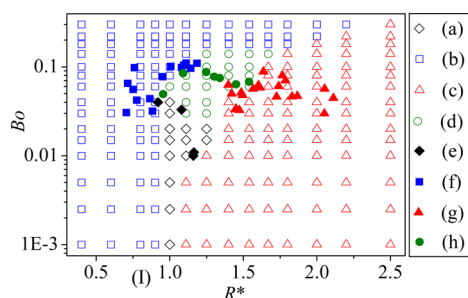


Figure 3. Phase diagram of the coalescence morphology transitions in droplet coalescence (symbols (a–d) indicate the numerical results of the coalescence types I, II-1, II-2, and III, and symbols (e–h) indicate the experimental results of coalescence types I, II-1, II-2, and III).

4. RESULTS AND DISCUSSION

4.1. Coalescence Behaviors. Herein, three different coalescence morphologies are observed during the entire droplet coalescence process. Note that, these results indicate that gravity turns to be increasingly pronounced in morphologies development of coalescences after the initial expansion of the liquid bridge, especially in the final pinch-off process. Therefore, we represent these three types of coalescence in the phase diagram in Figure 3, depending on the Bond number ($Bo = (\rho_l - \rho_a)gR^2/\sigma$ which characterizes the ratio of gravity to surface tension), and the dimensionless initial radius ratio of the pendent droplet to sessile one ($R^* = (R_{pi}/R_{si})$ which characterizes the size differences between the pendent and sessile droplets). These coalescence morphologies include coalescence with no pinch-off (type I) (Figure 4a and Movie S1, Supporting Information), coalescence with pinch-off

during the first necking stage (type II) (Figure 4b,c, Movie S2 and Movie S3), and coalescence with pinch-off during the second necking stage (type III) (Figure 4d and Movie S4). The coalescence with pinch-off during the first necking stage (type II) can be further classified into two subtypes: pinch-off at pendent droplet (type II-1) (Figure 4b and Movie S2) and pinch-off at the sessile droplet (type II-2) (Figure 4c and Movie S3).

By examining the current numerical results of velocity fields and pressure distribution under current coalescence morphologies, it is recognized that the onset and rapid motion of the liquid bridge (as illustrated in Figure 5a) at the initial stage of

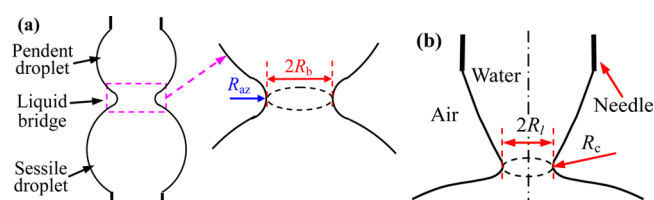


Figure 5. Schematic of droplet coalescence. (a) schematic of the liquid bridge; (b) schematic of the neck.

coalescence are attributed to the injection of liquid from the pendent and sessile droplets, which is driven by the capillary pressure difference established between the liquid bridge and two droplets (Δp_u and Δp_d in the inset of pressure distribution in Figure 4a-2). Meanwhile, interfacial energy of the two droplets is transformed into kinetic energy of the injecting fluid. With the further injection of liquid by the effect of inertia, the liquid bridge continues growing into a “nodule” with the neck

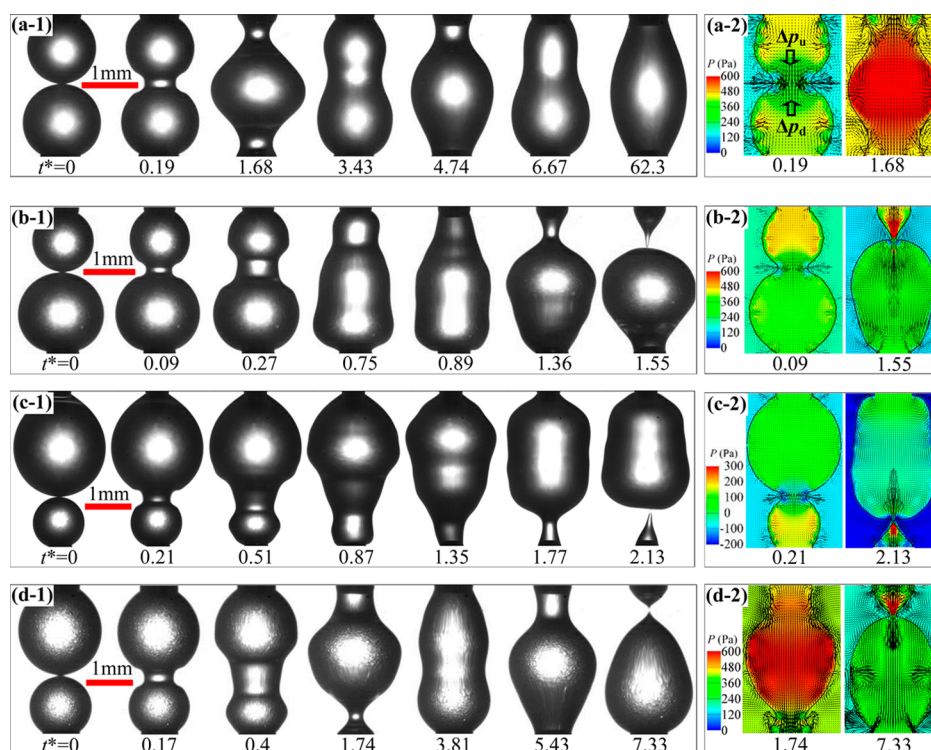


Figure 4. Coalescence of pendent and sessile droplets. (a) Type I ($Bo = 0.044$, $R^* = 0.92$): (a-1) experimental images, (a-2) pressure distribution and velocity profile. (b) Type II-1 ($Bo = 0.065$, $R^* = 0.71$): (b-1) experimental images, (b-2) pressure distribution and velocity profile. (c) Type II-2 ($Bo = 0.07$, $R^* = 1.79$): (c-1) experimental images, (c-2) pressure distribution and velocity profile. (d) Type III ($Bo = 0.075$, $R^* = 1.354$): (d-1) experimental images, (d-2) pressure distribution and velocity profile.

being formed between the needle tips and the “nodule” (Figure 4a), when the kinetic energy is transformed back into the interfacial energy of the “nodule” with the increasing interface area. Notably, starting from this stage, the topologies of coalescence exhibit distinct morphologies, which critically depend upon the early dynamics of coalescence and the net capillary force (Δp_n) at the necks,

$$\Delta p_n = 2\sigma(R_c^{-1} - R_l^{-1}) \quad (8)$$

where R_c^{-1} and R_l^{-1} are the azimuthal curvature and axial curvature of interface in the neck region, respectively (Figure 5b).

In the case of type I coalescence, the size of the pendent droplet is always close to that of sessile droplet, which produces little difference between Δp_u and Δp_d , resulting in similar necking rates and degrees at both pendent and sessile droplets. Consequently, draining at two necks stops almost simultaneously at the end of the first necking stage, with too little kinetic energy remaining to overcome the interfacial energy barrier of the neck interface for the pinch-off.²⁶ Moreover, the R_c^{-1} is observed to be sharper than R_l^{-1} at two necks, leading to a positive Δp_n , which enlarges the neck rather than squeezes it toward the pinch-off at first necking stage. Subsequently, the coalesced droplet appears to oscillate with decaying amplitude over time due to viscous dissipation. Finally, the coalesced droplet is suspended between the two needles assuming an olive shape ($t^* = 62.3$ in Figure 4a).

Compared with type I coalescence, type II coalescence is typically observed at a large size difference between the pendent and sessile droplets. Owing to the large size difference, a large pressure difference appears between Δp_u and Δp_d , leading to a faster drainage from the smaller drop to the liquid bridge than from the larger one. This creates a thin collapsing neck region with a small interface area, where the R_c^{-1} is essentially equal to the R_l^{-1} , suggesting no capillary driving force and a small energy barrier for the pinch-off. Therefore, the fluid inertia and high Bernoulli pressure at the neck drive the fluid draining from the neck while the remaining kinetic energy of fluid surmounts the energy barrier, thus inducing the final pinch-off (Figure 4b). It is demonstrated that gravity, which is always supposed to be negligible when Bo is less than 0.1,²⁷ actually enhances the fluid draining from the neck under the pinch-off at the pendent droplet (type II-1) and restrains that under the pinch-off at the sessile droplet (type II-2), leading to a faster pinch-off at the pendent droplet under similar size ratio between the two droplets as shown in Figure 4b,c.

Under the moderate size difference between the pendent and sessile droplets with respect to that of type II coalescence, type III coalescence comes out with the pinch-off at the second necking stage. Much like type I coalescence, type III also undergoes a first necking process; however, due to the initial size difference between the pendent and sessile droplets, an asymmetric interface oscillation occurs on the coalesced drop during the first necking process of coalescence, which is further amplified by the combined effects of inertia and interface tension at the second necking stage. As a result, a sharp shrinking of the upper neck emerges at this stage ($t^* = 5.43$ in Figure 4d), and subsequently induces the terminal pinch-off. As indicated by the phase diagram in Figure 3, the coalescence type III appears at a larger Bond number. Under the larger Bo , the effect of gravity plays a more important role on the droplet coalescence. During the first necking process of coalescence,

the gravity not only restrains the fluid draining from the neck, but also enhances the fluid in the pendent droplet flowing down to the sessile droplet. As a result, the neck at the sessile droplet cannot be thin enough to pinch off during the first necking process, as shown in Figure 4d-1. Then during the second necking process, a sharp shrinking of the upper neck emerges, and subsequently induces the terminal pinch-off; that is, the type III coalescence comes out.

Because of the significant impact of the difference in droplet size, and interaction of the surface tension and gravitational body forces on the hydrodynamic behaviors of drop coalescence, the coalescence morphologies described above can be represented quantitatively by a phase diagram that utilizes and compares R^* and Bo , as indicated in Figure 3.

4.2. Topography Evolution Analysis. It is important to note that the Ohnesorge number $Oh = \mu/(\rho\sigma R)^{1/2}$, which estimates the relative contributions of the viscous and inertial effects on the droplet coalescence driven by the surface tension,^{18,26–30} is 3.8×10^{-3} to 6.9×10^{-3} for the experimental cases and 0.5×10^{-3} to 7.3×10^{-3} for the numerical cases here. Therefore, the radius evolution of the liquid bridge R_b is dominated by the balance between surface tension and inertial force with a negligible role of viscous force, which can be quantitatively characterized by the following law:^{31,32}

$$R_b \sim \left(\frac{\sigma R}{\rho} \right)^{1/4} \sqrt{t} = R \sqrt{\frac{t}{t_c}} = R \sqrt{t^*} \quad (9)$$

where R_b is the radius of the liquid bridge. In addition to the well-documented linear inertial expansion of the liquid bridge versus $(t^*)^{1/2}$ at the moment of contact between the two droplets, the experimental and numerical investigations also provide the detailed temporal evolution of the liquid bridge during the following coalescence process (Figure 6). Interest-

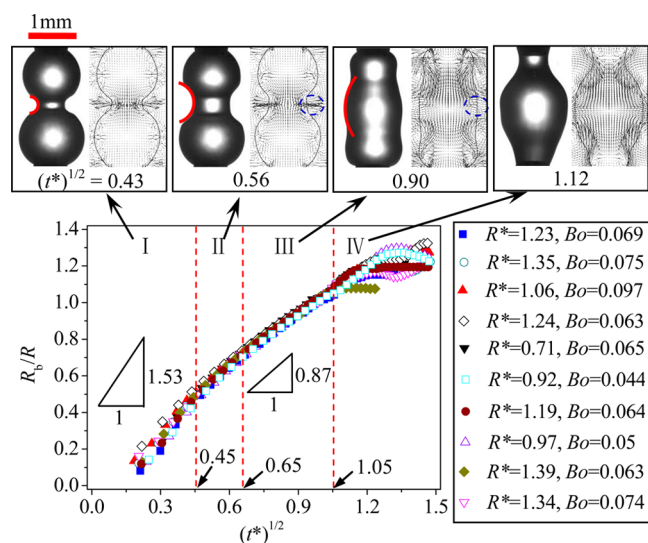


Figure 6. Evolution of dimensionless bridge radius versus the $(t^*)^{1/2}$ during the coalescence.

ingly, three distinct growth regimes of the liquid bridge are identified after the initial linear inertial expansion obeying the scaling law of $R_b/R \propto 1.53(t^*)^{1/2}$ prior to $(t^*)^{1/2} = 0.45$ (region I in Figure 6), one of which is a new linear growing with a smaller growth rate relative to the initial linear stage.

On the basis of the observation, the existence of these regimes can also be understood from the competition between capillary forces induced by azimuthal and axial curvatures of interface in the liquid bridge. During the initial linear inertial expansion stage, possessing a normal direction pointing to the axis of the bridge, the azimuthal surface of the bridge has a larger curvature than the axial one, thus producing a driving net capillary force for the expansion of the liquid bridge (marked image of $(t^*)^{1/2} = 0.43$ in Figure 6). With the extension of the bridge, the curvature of the azimuthal surface becomes smaller than the axial one. Although the component capillary pressure produced by the azimuthal surface of the bridge still plays a positive role in the bridge growth, the net capillary pressure turns to be negative, thereby slowing down the growth of the bridge (region II in Figure 6). In particular, after the transition region II, when the normal direction of azimuthal surface reaches a point outward from the surface, the capillary force generated by the azimuthal surface ceases to assist growth and actually begins to retard the growth of the liquid bridge (the marked image of $(t^*)^{1/2} = 0.90$ in Figure 6), which thereby generates a new slower expansion of the liquid bridge within the range of $0.65 < (t^*)^{1/2} < 1.05$ (region III in Figure 6). This new linear region is found to also follow a linear scaling law with a measured prefactor as $R_b/R \propto 0.87(t^*)^{1/2}$ (region III in Figure 6). Subsequently, owing to the propagation and superposition of the capillary wave inside the coalesced droplet, the liquid bridge exhibits an unstable behavior during evolution (region IV in Figure 6).

5. CONCLUSION

The combined experimental investigation and computational fluid dynamics (CFD) simulation are conducted to reveal the whole process of coalescence between pendent and sessile droplets. The interface evolution, including the evolution of neck and liquid bridge, involved in the coalescence are presented and analyzed. Several conclusions are obtained as follows:

- (1) Three typical coalescence morphologies, including coalescence with no pinch-off, coalescence with pinch-off during the first necking stage, and coalescence with pinch-off during the second necking stage, are identified in the entire coalescence process.
- (2) Gravity enhances the fluid draining from the neck under the pinch-off at the pendent droplet (type II-1) and restrains that under the pinch-off at the sessile droplet (type II-2), leading to a faster pinch-off at the pendent droplet under a similar size ratio between the two droplets.
- (3) Resulting from the transition of the capillary force produced by a change in the azimuthal surface profile of the liquid bridge, the evolution of liquid bridge can be divided into four distinct growth regimes, including a new linear but slower growth regime posterior to the well-known initial linear inertial expansion. This new linear growth is confirmed to follow a linear scaling law with a measured prefactor as $R_b/R \propto 0.87(t^*)^{1/2}$.

■ ASSOCIATED CONTENT

Supporting Information

The Supporting Information is available free of charge on the ACS Publications website at DOI: 10.1021/acs.iecr.5b01459.

Video demonstrating the coalescence morphology type I (Movie S1) (AVI)

Video demonstrating the coalescence morphology type II-1 (Movie S2) (AVI)

Video demonstrating the coalescence morphology type II-2 (Movie S3) (AVI)

Video demonstrating the coalescence morphology type III (Movie S4) (AVI)

■ AUTHOR INFORMATION

Corresponding Author

*Tel.: +86 514 87971809. Fax: +86 514 87311374. E-mail: chenyp@yzu.edu.cn.

Notes

The authors declare no competing financial interest.

■ ACKNOWLEDGMENTS

This work was supported by National Natural Science Foundation of China (No. 51222605) and National Natural Science Foundation of China – NSAF (No. U1530260).

■ REFERENCES

- (1) Yarin, A. L. Drop impact dynamics: splashing, spreading, receding, bouncing... *Annu. Rev. Fluid Mech.* **2006**, *38*, 159.
- (2) Rayleigh, L. On the Capillary Phenomena of Jets. *Proc. R. Soc. London* **1879**, *29*, 71.
- (3) Reynolds, O. On the Theory of Lubrication and Its Application to Mr. Beauchamp Tower's Experiments, Including an Experimental Determination of the Viscosity of Olive Oil. *Proc. R. Soc. London* **1886**, *177*, 157.
- (4) Zeff, B. W.; Kleber, B.; Fineberg, J.; Lathrop, D. P. Singularity dynamics in curvature collapse and jet eruption on a fluid surface. *Nature* **2000**, *403*, 401.
- (5) Bowen, E. G. The Formation of Rain by Coalescence. *Aust. J. Chem.* **1950**, *3*, 193.
- (6) Bhakta, A.; Ruckenstein, E. Decay of standing foams: drainage, coalescence and collapse. *Adv. Colloid Interface Sci.* **1997**, *70*, 1.
- (7) Singh, G.; Hirasaki, G. J.; Miller, C. A. Dynamics of foam films in constricted pores. *AIChE J.* **1997**, *43*, 3241.
- (8) Behjat, Y.; Shahhosseini, S.; Marvast, M. A. Modeling gas oil spray coalescence and vaporization in gas solid riser reactor. *Int. Commun. Heat Mass Transfer* **2010**, *37*, 935.
- (9) Šecarov-Sokolovic, R. M.; Vulic, T. J.; Sokolovic, S. M. Effect of fluid flow orientation on the coalescence of oil droplets in steady-state bed coalescers. *Ind. Eng. Chem. Res.* **2006**, *45*, 3891.
- (10) Nikolov, A. D.; Wasan, D. T. Effects of surfactant on multiple stepwise coalescence of single drops at liquid-liquid interfaces. *Ind. Eng. Chem. Res.* **1995**, *34*, 3653.
- (11) Aarts, D. G. A. L.; Lekkerkerker, H. N. W.; Guo, H.; Wegdam, G. H.; Bonn, D. Hydrodynamics of droplet coalescence. *Phys. Rev. Lett.* **2005**, *95*, 164503.
- (12) Fezzaa, K.; Wang, Y. Ultrafast x-ray phase-contrast imaging of the initial coalescence phase of two water droplets. *Phys. Rev. Lett.* **2008**, *100*, 104501.
- (13) Menchaca-Rocha, A.; Martinez-Davalos, A.; Nunez, R.; Popinet, S.; Zaleski, S. Coalescence of liquid drops by surface tension. *Phys. Rev. E: Stat. Phys., Plasmas, Fluids, Relat. Interdiscip. Top.* **2001**, *63*, 046309.
- (14) Wu, M. M.; Cubaud, T.; Ho, C. M. Scaling law in liquid drop coalescence driven by surface tension. *Phys. Fluids* **2004**, *16*, L51.
- (15) Case, S. C.; Nagel, S. R. Coalescence of low-viscosity liquids. *Phys. Rev. Lett.* **2008**, *100*, 084503.
- (16) Paulsen, J. D.; Burton, J. C.; Nagel, S. R. Viscous to inertial crossover in liquid drop coalescence. *Phys. Rev. Lett.* **2011**, *106*, 114501.
- (17) Case, S. C. Coalescence of low-viscosity fluids in air. *Phys. Rev. E* **2009**, *79*, 026307.

- (18) Paulsen, J. D.; Burton, J. C.; Nagel, S. R.; Appathurai, S.; Harris, M. T.; Basaran, O. A. The inexorable resistance of inertia determines the initial regime of drop coalescence. *Proc. Natl. Acad. Sci. U. S. A.* **2012**, *109*, 6857.
- (19) Yokota, M.; Okumura, K. Dimensional crossover in the coalescence dynamics of viscous drops confined in between two plates. *Proc. Natl. Acad. Sci. U. S. A.* **2011**, *108*, 6395.
- (20) Peng, B.; Wang, S.; Lan, Z.; Xu, W.; Wen, R.; Ma, X. Analysis of droplet jumping phenomenon with lattice Boltzmann simulation of droplet coalescence. *Appl. Phys. Lett.* **2013**, *102*, 151601.
- (21) Wang, F. C.; Yang, F.; Zhao, Y. P. Size effect on the coalescence-induced self-propelled droplet. *Appl. Phys. Lett.* **2011**, *98*, 053112.
- (22) Liao, Q.; Zhu, X.; Xing, S. M.; Wang, H. Visualization study on coalescence between pair of water drops on inclined surfaces. *Exp. Therm. Fluid Sci.* **2008**, *32*, 1647.
- (23) Li, J.; Renardy, Y. Y.; Renardy, M. Numerical simulation of breakup of a viscous drop in simple shear flow through a volume-of-fluid method. *Phys. Fluids* **2000**, *12*, 269.
- (24) Herrada, M. A.; Gañán-Calvo, A. M.; Ojeda-Monge, A.; Bluth, B.; Riesco-Chueca, P. Liquid flow focused by a gas: jetting, dripping, and recirculation. *Phys. Rev. E* **2008**, *78*, 036323.
- (25) Brackbill, J. U.; Kothe, D. B.; Zemach, C. A continuum method for modeling surface tension. *J. Comput. Phys.* **1992**, *100*, 335.
- (26) Yue, P.; Zhou, C.; Feng, J. J. A computational study of the coalescence between a drop and an interface in Newtonian and viscoelastic fluids. *Phys. Fluids* **2006**, *18*, 102102.
- (27) Blanchette, F.; Bigioni, T. P. Partial coalescence of drops at liquid interfaces. *Nat. Phys.* **2006**, *2*, 254.
- (28) Zhang, F. H.; Li, E. Q.; Thoroddsen, S. T. Satellite formation during coalescence of unequal size drops. *Phys. Rev. Lett.* **2009**, *102*, 104502.
- (29) Blanchette, F.; Bigioni, T. P. Dynamics of drop coalescence at fluid interfaces. *J. Fluid Mech.* **2009**, *620*, 333.
- (30) Aryafar, H.; Kavehpour, H. P. Drop coalescence through planar surfaces. *Phys. Fluids* **2006**, *18*, 072105.
- (31) Eggers, J.; Lister, J. R.; Stone, H. A. Coalescence of liquid drops. *J. Fluid Mech.* **1999**, *401*, 293.
- (32) Duchemin, L.; Eggers, J.; Josserand, C. Inviscid coalescence of drops. *J. Fluid Mech.* **2003**, *487*, 167.